CMS Physics Analysis Summary

Jet shapes based on two-particle angular correlations in PbPb collisions at $\sqrt{s_{\mathrm{NN}}} = 5.02$ TeV

The CMS Collaboration

Abstract

In ultrarelativistic heavy ion collisions, long- and short-range correlations can be studied by forming two-dimensional histograms of the separations in pseudorapidity and azimuth of each particle in an event with every other particle in that event, with the two particles forming a pair selected in specified transverse-momentum ranges. Averaged over many events, jets result in a well defined peak structure centered at zero separation in pseudorapidity and azimuth. This note explores the evolution of the two-particle jet peak shape with the pair transverse momentum ranges, the collision centrality, and the pseudorapidity of the jet peak. Lead-lead collision results at a center-of-mass energy per nucleon pair of 5.02 TeV are presented. The data were obtained using the CMS detector and correspond to an integrated luminosity of $0.607 \, \mathrm{nb}^{-1}$. Proton-proton collision data at the same nucleon-nucleon collision energy and corresponding to $252 \, \mathrm{nb}^{-1}$ are also presented to provide a vacuum reference. The results are discussed in terms of the boost invariance of the two-particle correlation jet peak shape.

1   Introduction

In ultrarelativistic heavy ion collisions, a deconfined state of quarks and gluons forms as the system reaches equilibrium, known as the quark-gluon plasma (QGP) [1, 2]. Jets are collimated streams of particles originating when partons, produced in high-momentum-transfer (hard) processes, fragment into lower-energy (softer) partons. These jets are produced during the pre-equilibrium stage of the collisions. As the jet shower evolves, the outgoing partons can interact with the QGP, leading to various physical phenomena collectively referred to as "jet quenching" [3]. Experimental evidence of jet quenching has been observed in many observables at RHIC [4, 5] and the LHC [6–9]. Jets serve as versatile tools for probing the properties of the QGP. A recent review of CMS measurements on this subject can be found in [6].

Two-particle correlations in pseudorapidity and azimuth offer a complementary method for studying jets in heavy ion collisions. They allow for simple background corrections, are sensitive to medium-induced modifications, reduce biases in jet reconstruction, and cover a broader range of jet energies and early-stage dynamics [10]. These correlations measure the relative separations in azimuth ($\Delta\phi$) and pseudorapidity ($\Delta\eta$) of a high-p_T "trigger" particle and lower-p_T associated particles. Jets appear as a concentrated "near-side" peak at ($\Delta\phi = 0$, $\Delta\eta = 0$). In these correlation plots, an elongated "away-side" structure in $\Delta\eta$ at $\Delta\phi = \pi$ is also typically present, corresponding to the recoil parton in a dijet event. CMS measurements in central lead-lead (PbPb) collisions reveal suppression on the away-side and moderate enhancement for the near-side correlation yields, indicating medium-induced modifications [10–12].

In relativistic heavy-ion collisions, "boost invariance," where particle behavior near mid-rapidity remains consistent despite the longitudinal motion of the colliding nucleons, has been observed [13]. However, this symmetry may weaken at forward rapidity due to the increasing influence of longitudinal dynamics in the system. This makes the forward region particularly interesting, as it probes extreme kinematic conditions where initial-state effects, such as parton saturation, become more pronounced and potentially challenge the assumption of boost invariance. Additionally, studying high-p_T particles, where $\eta \approx y$, offers a unique opportunity to test whether boost invariance extends beyond the bulk medium into the hard-scattering regime of QCD, providing insights into both the soft and perturbative sectors of particle production.

This analysis examines the angular distribution of associated particles relative to a trigger particle across the wide rapidity range of the CMS detector ($|\eta| < 2.4$). The PbPb collision data is obtained at a center-of-mass energy per nucleon pair of $\sqrt{s_{NN}} = 5.02$ TeV. Results are also reported for pp collisions at the same nucleon-nucleon collision energy to provide a vacuum reference. Using two-particle correlations, we extract the longitudinal ($\Delta\eta$) and transverse ($\Delta\phi$) widths of the near-side jet peak shape. Additionally, we investigate the rapidity-dependent boost invariance of this peak shape for higher-momentum trigger particles.

2   Experimental setup and data sample

The central feature of the CMS apparatus is a superconducting solenoid of 6 m internal diameter, providing a magnetic field of 3.8 T. Within the solenoid volume there are silicon and strip tracking detectors, a lead tungstate crystal electromagnetic calorimeter and a brass and scintillator hadron calorimeter, each composed of a barrel and two endcap sections. The silicon tracker consists of 1440 silicon pixel and 15,148 silicon strip detector modules. A new pixel tracker was installed in 2017 to increase the tracking acceptance by adding active layers in both central and end-cap regions. The CMS Phase-1 pixel detector is built from 1856 segmented silicon sensor modules, where 1184 modules are used in the barrel pixel detector and 672 modules

are used for the forward disks. Each module consists of a sensor with 160×416 pixels connected to 16 readout chips. Tracker Inner Barrel and Tracker Outer Barrel contain 512 strips per module. Tracker Endcap and Tracker Inner Disks can have modules with up to 768 strips per module. The tracker detector measures the charged particles within the range $|\eta| < 3.0$ [14–16]. The forward hadron (HF) calorimeter uses steel as an absorber and quartz fibers as the sensitive material. The two halves of the HF are located $11.2\,\text{m}$ from the interaction region, one on each end, and together they provide coverage in the range $3.0 < |\eta| < 5.2$. The HF calorimeters are subdivided into "towers" with $\Delta\eta \times \Delta\phi = 0.175 \times 0.175$, and energy deposited in a tower is treated to centrality determination in this analysis. They also serve as luminosity monitors. A more detailed description of the CMS detector, together with a definition of the coordinate system used and the relevant kinematic variables can be found in Ref. [17].

The analysis presented in this note is based on PbPb (pp) collisions at $\sqrt{s_{\text{NN}}} = 5.02\,\text{TeV}$ collected by the CMS experiment in 2018 (2017). Approximately 4.27×10^9 PbPb events and 15 billion pp events were used, corresponding to an integrated luminosity of $0.607\,\text{nb}^{-1}$ [18, 19] and $252\,\text{nb}^{-1}$, respectively. The data samples were collected by the CMS experiment with a two-tiered trigger system. The first level trigger (L1) consists of custom hardware processors and uses information from the calorimeters and muon detectors to select events at a rate of around $100\,\text{kHz}$ within a fixed latency of about $4\,\mu\text{s}$ [20]. The second level or high-level trigger (HLT) consists of a farm of processors running a version of the full event reconstruction software optimized for fast processing, and reduces the event rate to around $1\,\text{kHz}$ before data storage [21]. The Minimum Bias (MB) events are triggered by requiring signals above thresholds in the range of $\sim 6 - 12\,\text{GeV}$ in both sides of the HF calorimeters [21]. Further selections are applied offline to reject events from background processes (beam-gas interactions and nonhadronic collisions), as discussed in Ref. [22]. In the offline analysis, events are required to have at least one interaction vertex, based on two or more reconstructed tracks, with a distance of less than $15\,\text{cm}$ from the center of the nominal interaction point along the beam axis, z_{vtx}. The primary vertex (PV) is taken to be the vertex corresponding to the highest track multiplicity in the event, evaluated using tracking information alone, as described in Section 9.4.1 of Ref. [23]. In the final analysis, the PbPb collision events are required to have at least two calorimeter towers in each HF detector with energy deposits of more than $4\,\text{GeV}$ per tower. These criteria select $(99 \pm 2)\%$ of inelastic hadronic PbPb collisions. Finding values higher than 100% reflects the possible presence of ultra-peripheral (nonhadronic) collisions in the selected event sample.

The selected tracks are corrected for tracking inefficiency and acceptance using simulated Monte Carlo samples calculated using PYTHIA 8.212 [24] with the CP5 tune [25] for pp collisions, and HYDJET 1.9 [26] for PbPb collisions. Unless otherwise specified, PYTHIA8 refers to the CP5 tune throughout this note. The response of the CMS detector to these simulated events is modeled using GEANT4 [27].

3   Analysis procedure

For this analysis, charged tracks are selected within $|\eta| < 2.4$, provided that the significance of the reconstructed longitudinal distance (d_z) and transverse distance (d_{xy}) from the beam axis satisfy $|d_z|/\sigma_z < 3.0$ and $|d_{xy}|/\sigma_{xy} < 3.0$, where σ_z and σ_{xy} represent the measurement uncertainties. Additionally, the transverse momentum resolution for each track, expressed as σ_{p_T}/p_T, must be less than 10%. The number of tracker hits on each track should be no fewer than 11, and the reduced chi-squared of the track fit ($\chi^2/N_{\text{dof}}/N_{\text{layers}}$) must be below 0.18. These conditions define the nominal track selection criteria.

3.1 Longitudinal and transverse width of the near-side peak

The correlation between two charged particles is calculated as a function of the azimuth difference $\Delta\phi$ (defined between $-\pi/2$ and $3\pi/2$) and pseudorapidity difference $\Delta\eta$. The correlation is expressed in terms of the associated yield per trigger particle for intervals of the trigger and associated transverse momentum, $p_{\mathrm{T,trig}}$, and $p_{\mathrm{T,assoc}}$. The number of trigger particles for each event is denoted by N_{trig}, which is corrected for tracking efficiency and the fake rate. The signal distribution, $S(\Delta\eta, \Delta\varphi)$, is constructed from pairs of particles within the same event and is normalized by the number of trigger particles, where N^{same} is the number of pairs in the $(\Delta\eta, \Delta\varphi)$ bin. Here, $\Delta\eta$ and $\Delta\varphi$ represent the difference in pseudorapidity and the difference in relative azimuthal angle between the two particles that form the pair [28–30].

$$S(\Delta\eta, \Delta\varphi) = \frac{1}{N_{\mathrm{trig}}} \frac{d^2 N^{\mathrm{same}}}{d\Delta\eta\Delta\varphi} \tag{1}$$

Much of the two-particle correlations observed in heavy-ion collisions are influenced by the underlying event, which consists of the overall background of particle production and random combinatorial effects rather than direct interactions between particles. To accurately separate this background from genuine physical correlations, the mixed event distribution is employed as a reference. The mixed event distribution $B(\Delta\eta, \Delta\varphi)$ is constructed by pairing the trigger particles in each event with the particles from ten random events [28–30]. Events are mixed only if they are within the same centrality (in PbPb) or track multiplicity (in pp) range, and the relative difference of the primary vertex along the z-axis is less than 2 cm. Thus, the mixed event distribution is defined as

$$B(\Delta\eta, \Delta\varphi) = \frac{1}{N_{\mathrm{trig}}} \frac{d^2 N^{\mathrm{mix}}}{d\Delta\eta\Delta\varphi} \tag{2}$$

where N^{mix} is the number of mixed event pairs in a given $(\Delta\eta, \Delta\varphi)$ bin [11, 28–32]. The per-trigger-particle associated yield is defined as

$$\frac{1}{N_{\mathrm{trig}}} \frac{d^2 N^{\mathrm{pair}}}{\Delta\eta\Delta\varphi} = C_2(\Delta\eta, \Delta\varphi) = B(0,0) \frac{S(\Delta\eta, \Delta\varphi)}{B(\Delta\eta, \Delta\varphi)} \tag{3}$$

The signal distribution in the left plot of Fig. 1 has real physical correlations, while the mixed event distribution in the middle plot of Fig. 1 does not contain physics information. However, the mixed event distribution is used to exclude the detector effects present in the signal distribution. Therefore, the ratio $\frac{B(0,0)}{B(\Delta\eta,\Delta\varphi)}$ accounts for the pair-acceptance correction factor used to derive the corrected per-trigger particle-associated yield distribution, which is shown in the right plot of Fig. 1 [11, 28–32].

We perform a two-dimensional fitting technique, as shown in Fig. 2, which includes the peak itself and the long-range correlation background resulting from collective effects [33] in order to characterize the near-side peak shape, as seen in Fig. 3. This approach utilizes the fact that long-range correlation structures are mostly independent of $\Delta\eta$, while the near-side peak in two-particle correlations is concentrated around $\Delta\phi = 0$, $\Delta\eta = 0$. However, because the away-side peak is elongated in $\Delta\eta$, the away side cannot be studied using this method [31, 34]. The fit
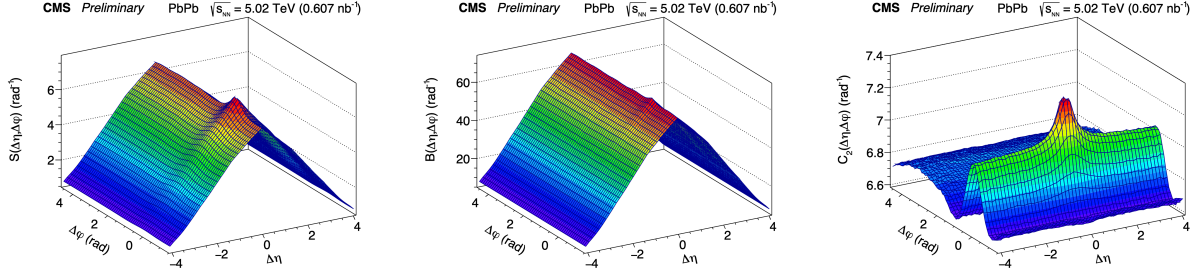
Figure 1: Signal distribution (left), mixed event distribution (middle), correlation function (right) for 0-10% centrality, $3.0 < p_{T,trig} < 4.0\,\text{GeV}$ and $2.0 < p_{T,asso} < 3.0\,\text{GeV}$ in PbPb collisions data at 5.02 TeV.

function consists of a constant, a generalized two-dimensional Gaussian function [31, 32, 34], and $\cos(n\Delta\phi)$ terms for $n = 2, 3,$ and 4.

$$F(\Delta\phi, \Delta\eta) = c_1[1 + \sum_{n=2}^{4} 2V_{n\Delta}\cos(n\Delta\phi)] + c_2 G_{\gamma_{\Delta\phi},\omega_{\Delta\phi}} G_{\gamma_{\Delta\eta},\omega_{\Delta\eta}} \tag{4}$$

$$G_{\gamma_x,\omega_x}(x) = \frac{\gamma_x}{2\omega_x\Gamma(1/\gamma_x)}exp\left[-\left(\frac{|x|}{\omega_x}\right)^{\gamma_x}\right]. \tag{5}$$
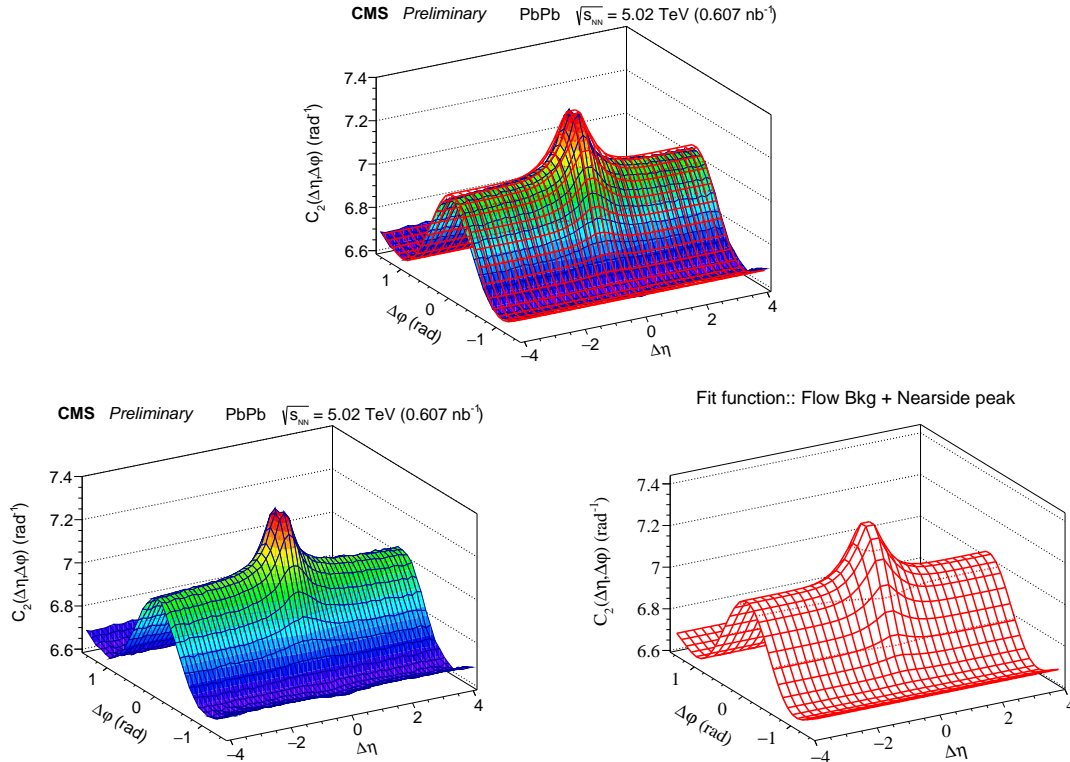

Figure 2: 2D correlations + 2D Fit functions (upper panel), 2D correlations (lower panel: left), 2D Fit function (lower panel: right) for 0–10% centrality, $3.0 < p_{T,trig} < 4.0\,\text{GeV}$ and $2.0 < p_{T,asso} < 3.0\,\text{GeV}$ in PbPb collisions data at 5.02 TeV.

Four components (c_1, $V_{n\Delta}$), where $V_{n\Delta}$ denotes the Fourier components linked to long-range correlations, parameterize the background in PbPb collisions. Importantly, the fit results re-
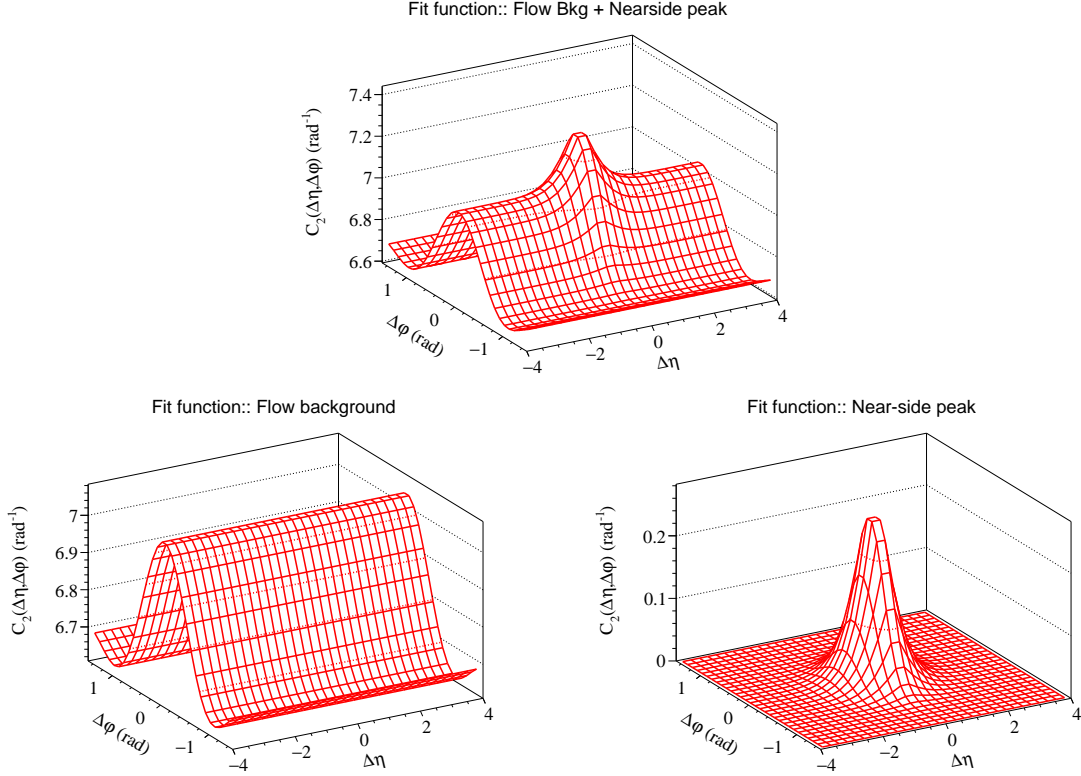
Figure 3: 2D Fit functions (upper panel), Flow background fit (lower panel: left), Near-side 2D peak fit (lower panel: right) for 0–10% centrality, $3.0 < p_{\mathrm{T,trig}} < 4.0\,\mathrm{GeV}$ and $2.0 < p_{\mathrm{T,asso}} < 3.0\,\mathrm{GeV}$ in PbPb collisions.

main largely unaffected by including higher-order components beyond the fourth. In contrast, the constant c_1 primarily characterizes the background for pp collisions. This study focuses on the shape of the near-side peak. Although this shape is described by four parameters ($\gamma_{\Delta\phi}$, $\omega_{\Delta\phi}$, $\gamma_{\Delta\eta}$, and $\omega_{\Delta\eta}$) and an overall normalization c_2, we calculate the second moments along the $\Delta\phi$ and $\Delta\eta$ axes: $\sigma^2_{\Delta\phi}$ and $\sigma^2_{\Delta\eta}$.

$$\sigma_x = \sqrt{\frac{\omega_x^2\,\Gamma(3/\gamma_x)}{\Gamma(1/\gamma_x)}} \tag{6}$$

Here, x stands for $\Delta\phi$ and $\Delta\eta$.

The one dimensional (1D) fitting on projection of $\Delta\phi$ and $\Delta\eta$ is explored using the function listed in Eq. 7 and Eq. 8 respectively.

$$F(\Delta\phi) = c_1[1 + \sum_{n=2}^{4} 2V_{n\Delta}\cos(n\Delta\phi)] + c_2\,G_{\gamma_{\Delta\phi},\omega_{\Delta\phi}} \tag{7}$$

$$F(\Delta\eta) = c_1 + c_2\,G_{\gamma_{\Delta\eta},\omega_{\Delta\eta}} \tag{8}$$

Clearly, the fit function does not adequately describe the long-range portion of the $\Delta\eta$ shape in the 2D fit. Fig. 4 shows the 1D $\Delta\eta$ and $\Delta\phi$ projections with the fit function.
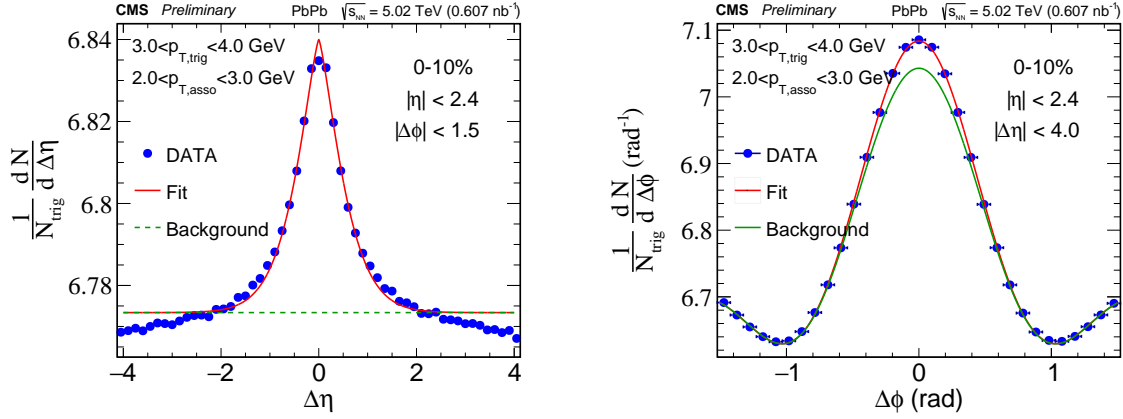
Figure 4: 1D $\Delta\eta$(left) and $\Delta\phi$(right) projection fit.

To address the issues with long-range background contributions, we introduce a different approach in which we fit the full $\Delta\eta$ region ($|\Delta\eta| < 4.0$) with two components: a generalized Gaussian function to describe the near-side peak region and a standard Gaussian function to capture the long-range $\Delta\eta$-dependent background. Both components are fitted simultaneously, as shown in Fig. 5. The width from the generalized Gaussian is considered as the nominal near-side width. Additionally, one of the systematic uncertainties is derived from an alternative fitting approach, which is discussed in Section 4.
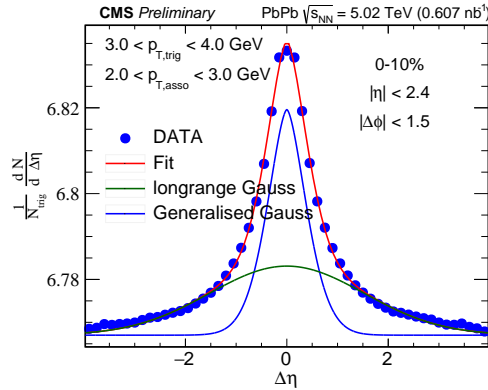

Figure 5: 1D fit of $\Delta\eta$ including one generalized Gaussian (blue) and a standard Gaussian (green) in the range $|\Delta\eta| < 4.0$.

3.2 Longitudinal asymmetry of the near-side peak from mid to forward rapidity

To investigate boost invariance, the asymmetry in the near-side jet peak structure found using two-particle correlations is explored as a function of pseudorapidity. Since, in most cases, the energy of the produced particles is much higher than their mass, pseudorapidity is used instead of rapidity. Moreover, the scaling behavior of particle production demonstrates that distributions such as $dN/d\eta$ exhibit smoother behavior across various collision energies compared to dN/dy [35]. This scaling behavior supports the use of η as a reliable variable for analyzing particle production, especially in contexts where longitudinal boost invariance is being investigated. The analysis is performed for eight trigger η ranges, with bin boundaries [–2.0,–1.5,–1.0,–0.5,0,0.5,1.0,1.5,2.0]. The corresponding two-particle correlations, $C_2(\Delta\eta, \Delta\phi)$ are normalized by the number of trigger particles to obtain the associated yield per trigger in each trigger η region. For a symmetric system, such as the PbPb system, there should be a mirror

symmetry with, e.g., the distribution for $1.5 < \eta_{\mathrm{trig}} < 2.0$ is the mirror image of the distribution for $-2.0 < \eta_{\mathrm{trig}} < -1.5$. This is illustrated with the upper left and lower left figures in Fig. 6. We take the average of the C_2 distributions for $\eta_{\mathrm{trig}} > 0.0$ and the mirror image of C_2 for $\eta_{\mathrm{trig}} < 0.0$, as shown in the lower right figure in Fig. 6. Whether boost invariance holds can be determined by measuring the associated yield per trigger for $\Delta\eta > 0$ and $\Delta\eta < 0$, and quantifying this longitudinal asymmetry by calculating the associated yield ratio.

Figure 6 shows the near-side 2D peak for triggers particles within a pseudorapidity range of $1.5 < |\eta_{\mathrm{trig}}| < 2.0$ and associated particles within a pseudorapidity range of $-2.4 < \eta_{\mathrm{asso}} < 2.4$. The transverse momentum ranges for the trigger and associated particles are $4.0 < p_{\mathrm{T,trig}} < 8.0\,\mathrm{GeV}$ and $2.0 < p_{\mathrm{T,asso}} < 3.0\,\mathrm{GeV}$, respectively. From these 2D correlations, we create 1D projections in $\Delta\eta$ within $|\Delta\phi| < 1.0$ (see Fig. 7) to calculate the trigger-normalized associated yield and quantify the trigger-normalized associated yield asymmetry in the longitudinal direction (longitudinal asymmetry) from the ratio of yields with $\Delta\eta > 0$ to $\Delta\eta < 0$.
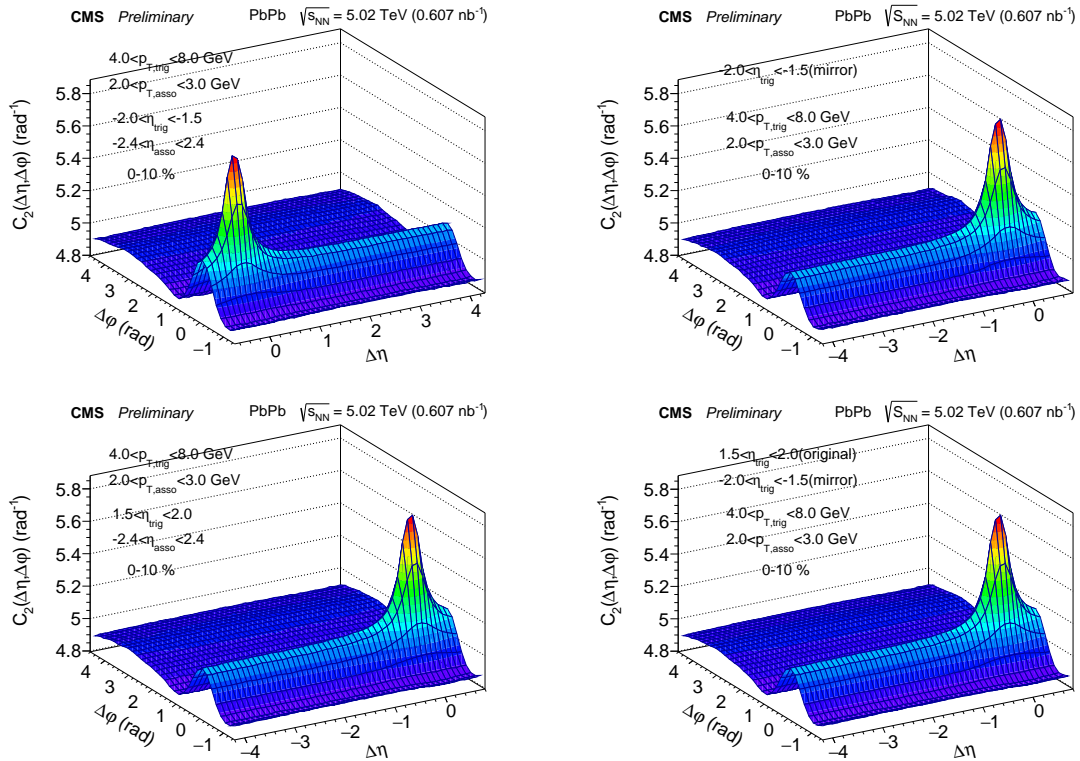

Figure 6: 2D correlation of $1.5 < |\eta_{\mathrm{trig}}| < 2.0$. In upper panel: the left plot (first) corresponds to $-2.0 < \eta_{\mathrm{trig}} < -1.5$, the right plot (second) is the mirror image of the first . In lower panel: the left plot (third) is for $1.5 < \eta_{\mathrm{trig}} < 2.0$, and the right plot (fourth) is the average of the second and the third plots.

In Fig. 7, to calculate the yield ratio, we first determine an offset based on the minimum value of the distribution. This offset is subtracted from the entire distribution to set the minimum value to zero. By performing this offset subtraction, we disentangle the near-side peak from the constant background, ensuring that the measured yield includes only the contribution from the near-side peak. We then consider the $\Delta\eta$ range from 0.0 to 0.7 on the right side and from -0.7 to 0.0 on the left side, using seven bins on each side of $\Delta\eta = 0.0$. This $\Delta\eta$ range is maintained for all η_{trig} bins ($0.0 < |\eta_{\mathrm{trig}}| < 0.5$, $0.5 < |\eta_{\mathrm{trig}}| < 1.0$, $1.0 < |\eta_{\mathrm{trig}}| < 1.5$, $1.5 < |\eta_{\mathrm{trig}}| < 2.0$). The associated yield asymmetry is taken as the yield ratio $Y_{\Delta\eta>0.0} / Y_{\Delta\eta<0.0}$.
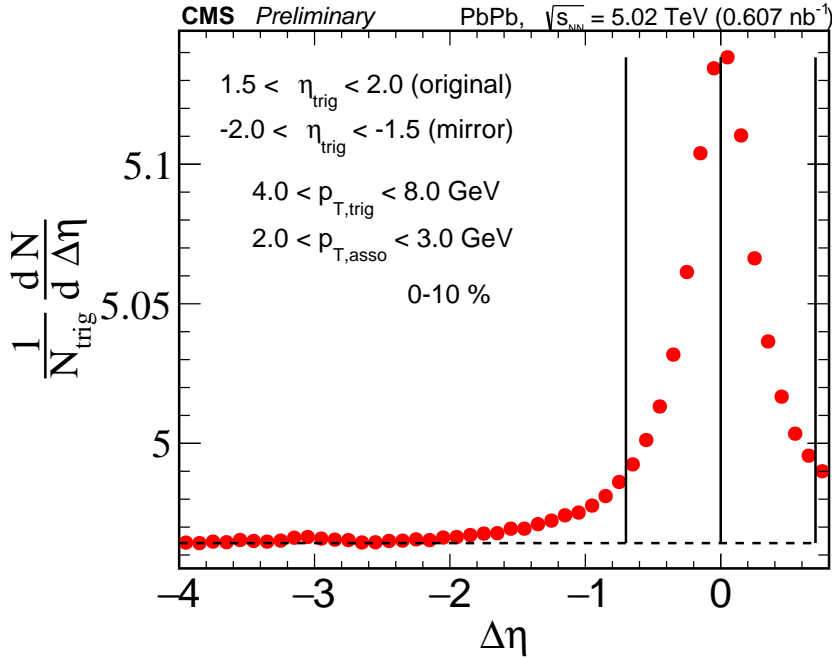
Figure 7: 1D $\Delta\eta$ projection from the averaged 2D correlation, combining $1.5 < \eta_{\text{trig}} < 2.0$ (original) and $-2.0 < \eta_{\text{trig}} < -1.5$ (mirror).

4 Systematic uncertainties

Systematic uncertainties are calculated by varying the event and track selections for both PbPb and pp collision events. The near-side jet peak widths and yields are calculated for three ranges of the vertex position in z (v_z) of PV to account for any acceptance effects: $|v_z| < 3$ cm, $-15 < v_z < -3$ cm, and $3 < v_z < 15$ cm, where the nominal z-vertex range is $-15 < v_z < 15$ cm. The maximum absolute systematic uncertainties due to the v_z cuts are around 0.03. High-quality tracks are selected according to the offline selection discussed in Section 3. These selection cuts are varied to investigate possible effects on the final measurements. The ranges are adjusted by changing $|d_z|/\sigma_z$ and $|d_{xy}|/\sigma_{xy}$ from 2 to 5, σ_{p_T}/p_T from 0.05 to 0.15, and the normalized χ^2 from 0.15 to 0.18. These track quality variations are crucial because they directly impact the precision of the reconstructed tracks and, consequently, the measurements of jet peaks. The maximum absolute systematic uncertainties due to the track cuts are around 0.02. Moreover, the centrality calibration is varied to estimate the related systematic uncertainty in the width of the near-side peak for PbPb collisions. This variation is necessary because widths and associated yield ratios both are estimated as a function of centrality. It has a maximum absolute systematic difference of around 0.01. The pileup effect is negligible in PbPb and is only studied in pp collisions by varying the pileup selection of events by considering the distance among reconstructed vertices and their associated number of tracks. The maximum effect due to pileup in pp is around 0.01. The correction factor used for tracking efficiency has an associated uncertainty of 5%. Within this range, tracking efficiency is also varied and considered a systematic source. Though its impact is negligible.

In a different fitting approach, we consider a systematic source in which we first fit the long-range correlation with a standard Gaussian from the sideband regions, where the short-range correlation contribution is assumed to be negligible. Then, in the second step, we fit the near-side peak with a generalized Gaussian on top of the extended contribution of the sideband

Systematic Sources	$\sigma_{\Delta\eta}$	$\sigma_{\Delta\phi}$	$Y_{\Delta\eta>0.0}/Y_{\Delta\eta<0.0}$
Vertex z	$0.000 - 0.014$	0.000	$0.002 - 0.033$
Track requirements	$0.000 - 0.010$	$0.000 - 0.001$	$0.000 - 0.017$
Centrality table	$0.001 - 0.010$	$0.000 - 0.004$	$0.000 - 0.013$
Pileup (for pp)	$0.001 - 0.006$	$0.000 - 0.005$	$0.001 - 0.014$
Tracking efficiency	$0.000 - 0.003$	$0.000 - 0.001$	$0.000 - 0.004$
Sideband fit	$0.001 - 0.084$	$-$	$-$
η_{trig} side	$-$	$-$	$0.000 - 0.004$
Total uncertainty	$0.003 - 0.086$	$0.001 - 0.004$	$0.002 - 0.037$

Table 1: Summary of the absolute systematic uncertainties for $\sigma_{\Delta\eta}$, $\sigma_{\Delta\phi}$, and the associated yield ratio. The leftmost column lists all systematic sources, while the other columns show the range of systematic uncertainties across all centrality bins in PbPb and pp MB.

Gaussian. This approach restricts the long-range effect to the sideband regions, and the nature of the systematic shift is unidirectional. Therefore, we consider an asymmetric uncertainty for this source. It introduces a maximum systematic uncertainty of approximately 0.08. A comparison of the near-side peak $\Delta\eta$ width using the systematic approach (sideband fit) with $|\eta| < 2.4$ and using a 2D fit with $|\eta| < 0.8$ can be found in Fig. 11 in Appendix B.

Longitudinal asymmetry studies are performed on the averaged 2D correlation of $\eta_{\text{trig}} > 0.0$ and the mirror $\eta_{\text{trig}} < 0.0$. We also perform separate studies of each $\eta_{\text{trig}} > 0.0$ and the mirror of $\eta_{\text{trig}} < 0.0$ as systematic sources. Its effect on the systematic uncertainty is around 0.04.

The nominal $\Delta\eta$ ranges for the yield measurement are defined as $(0.0 - 0.7)$ and $(- 0.7 - 0.0)$ for the $\Delta\eta > 0.0$ and $\Delta\eta < 0.0$ axes, respectively. For the systematic variations, two ranges are considered, once 0.7 is adjusted to 0.8, another 0.7 is adjusted to 0.6.

The systematic uncertainties for each source are estimated from the difference between the measurements with nominal and varied selections. The maximum variation for each source is taken as the final systematic uncertainty, and the total systematic uncertainty is evaluated by adding all the uncertainties in quadrature. Table 1 summarizes the systematic uncertainties from different sources for v_z, variation of track requirements, centrality table, pileup, tracking efficiency, sideband fixed fitting, and η_{trig} direction. The systematic uncertainty due to the tracking efficiency is minimal, and the uncertainty due to the $\Delta\eta$ range for the longitudinal associated yield asymmetry observable is negligible and therefore not considered. The dominant systematic source is the vertex position in z. In contrast, the statistical uncertainties for the longitudinal and transverse widths are less compared to the marker size, while those for the associated yield ratios are comparable to the systematic uncertainties.

5 Results

Figure 8 shows the longitudinal and transverse widths as a function of centrality in the different p_T ranges of the triggered and the associated particles. It is observed that the near-side peak shape has similar widths in $\Delta\eta$ and $\Delta\phi$ for pp collisions and PbPb collisions in the large centrality range (50–80%), commonly referred to as peripheral collisions. However, this symmetric trend vanishes in longitudinal widths toward central collisions. The $\Delta\eta$ with is found to increase towards central collisions, and this longitudinal broadening is most pronounced for low-p_T trigger and associated particle ranges. Maximal longitudinal broadening is observed at trigger-p_T 3–4 GeV and associate-p_T 2–3 GeV. Very little, if any, centrality-dependent broaden-
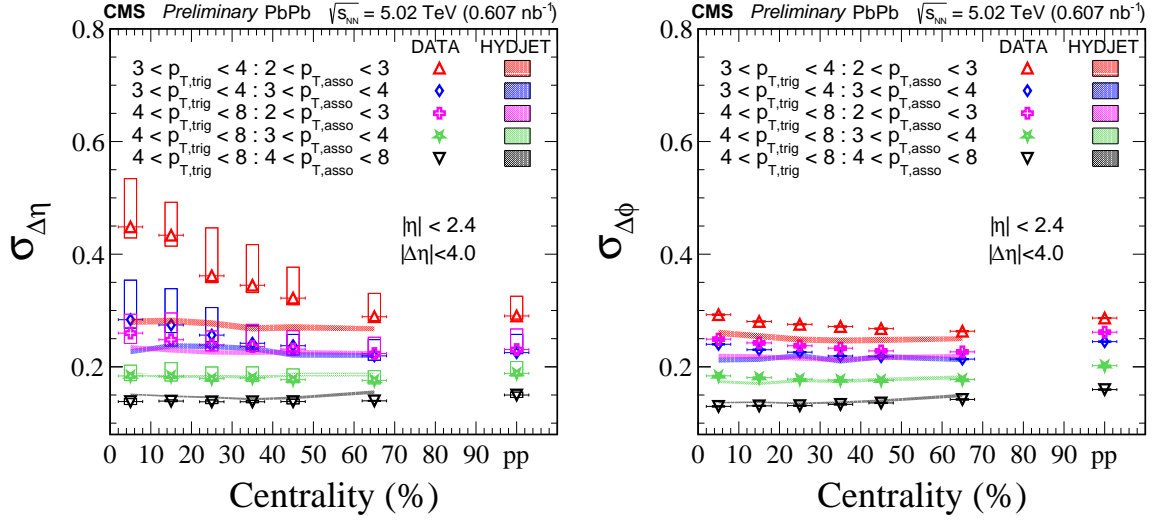
Figure 8: Longitudinal width $\sigma_{\Delta\eta}$ (left panel) and transverse width $\sigma_{\Delta\phi}$ (right panel) as a function of centrality in different p_T ranges for PbPb collisions and pp collisions (rightmost points in each panel). The statistical uncertainties of the data points are smaller than the marker size, and rectangular boxes indicate the systematic uncertainties. The dashed lines represent the expectation from the HYDJET 1.9 Monte Carlo event generator.

ing is observed as a function of $\Delta\phi$. In contrast, HYDJET predicts that both the longitudinal and transverse jet peak shape widths are nearly independent of the centrality. A possible explanation for these results is that longitudinal hydrodynamic flow deforms the jet shape as the jet interacts with the longitudinal flow of the QGP medium. Alternatively, the observed behavior could result from energy loss of the progenitor parton of the trigger hadron in passing through the QGP medium.

If the same particle acceptance ($|\eta| < 0.8$) as in earlier ALICE results [34] is used, good agreement is found, as illustrated in Fig. 10 in Appendix A. Moving to higher rapidity introduces long-range contributions that affect the observed jet structure. These contributions may arise from the interplay of multiple scattering processes and hydrodynamic effects in the medium, leading to modifications in the shape of the near-side peak.

Figure 9 shows the associated yield ratio between $\Delta\eta > 0$ and $\Delta\eta < 0$, measured as a function of centrality for different p_T ranges of triggered (top row) and associated (bottom row) particles. The measurement is also presented (Fig. 9, left to right) in the η bins of the triggered particles. The result for pp data is shown in the last bin of each plot. A significant increase in the associated yield ratio is observed as the analysis moves toward forward pseudorapidity (high η_{trig}). At mid pseudorapidity (low η_{trig}), the associated yield ratio is consistent with unity and almost independent of $p_{T,\text{trig}}$ and $p_{T,\text{asso}}$, within their respective uncertainties. However, at high η_{trig}, a slight dependence on $p_{T,\text{trig}}$ is observed across centrality, where the asymmetry increases toward central collisions. One possible explanation for the higher associated yield for $\Delta\eta > 0$ (where η_{trig} is always positive by choice) is that a longitudinally expanding medium might impart additional thrust to the high-momentum trigger jet, potentially leading to more associated particles in the forward direction through a recombination process.
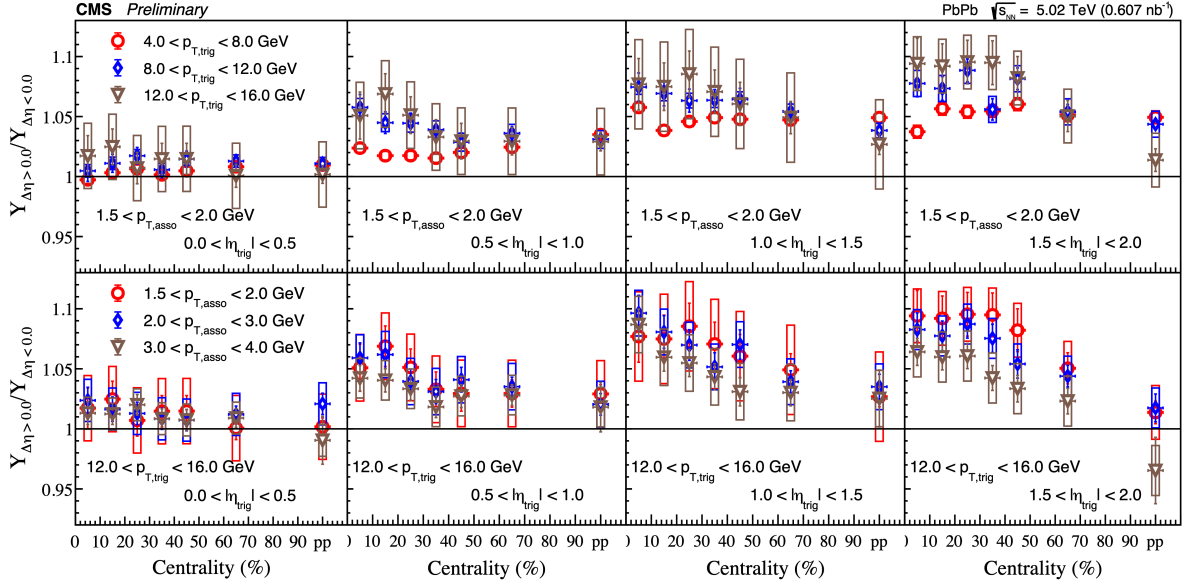
Figure 9: Associated yield ratios between $\Delta\eta > 0.0$ and $\Delta\eta < 0.0$ within the range of $0.0 < |\Delta\eta| < 0.7$ as a function of centrality in different p_T and η_{trig} ranges for PbPb collisions and pp collisions (rightmost bin) are presented in the upper two panels. Each panel (upper and lower) consists of four plots, each corresponding to a different value of η_{trig}. In the top panel, each plot consists of three colored markers representing different $p_{T,trig}$ values ($4 < p_{T,trig} < 8$, $8 < p_{T,trig} < 12$, $12 < p_{T,trig} < 16$ GeV), while $p_{T,asso}$ is fixed ($1.5 < p_{T,asso} < 2$ GeV). In the bottom panel, each plot consists of three colored markers representing different $p_{T,asso}$ values ($1.5 < p_{T,asso} < 2$, $2 < p_{T,asso} < 3$, $3 < p_{T,asso} < 4$ GeV), while $p_{T,trig}$ is fixed ($12 < p_{T,trig} < 16$ GeV). The rectangular open boxes represent the systematic uncertainties, while the vertical bars indicate the statistical uncertainties.

6 Summary

The centrality and pseudorapidity dependencies of jet peak shapes are explored using two-particle correlations. Lead-lead collision data at a center-of-mass energy per nucleon pair of 5.02 TeV were obtained using the CMS detector. These minimum-bias data correspond to an integrated luminosity of $0.607\,\text{nb}^{-1}$. Proton-proton collision data at the same nucleon-nucleon collisions energy are also shown to provide a vacuum reference. Particles detected in one transverse-momentum range are correlated with all particles in an event within a second range. The separations in pseudorapidity and azimuth of particles within each two-particle pair are then averaged over all events. Jets result in a peak shaped structure corresponding to pairs where there is a minimal separation of particles. The widths in pseudorapidity and azimuth of the jet peak shape are presented as functions of centrality and pseudorapidity. The skewness of the jet peak shape as a function of pseudorapidity is also explored by taking ratios of yields on the two sides of the peak.

For PbPb collisions, the widths of the jet peak azimuth distributions are found to be nearly independent of collision centrality, and are comparable to those in the pp reference distribution. Similarly, when one of the particles in each PbPb collision pair has a high transverse momentum, with $p_T > 4$ GeV, the jet peak pseudorapidity distributions also show little dependence on centrality and remain consistent with the pp reference distribution. However, when the high-p_T particle in each PbPb pair is restricted to a relatively low momentum range of $3 < p_T < 4$ GeV, an enhancement is found in the pseudorapidity width that increases as collisions become more

central. In this case, the pseudorapidity width only agrees with the pp reference for the most peripheral events. These results might be explained either by the influence of longitudinal hydrodynamic flow on the pseudorapidity width or by the progenitor parton losing energy while passing through the medium.

The skewness of the jet peak distribution in the particle pseudorapidity difference is studied by taking the ratio of yields on either side of the jet peaks. This ratio is determined in different, non-overlapping pseudorapidity ranges for the higher p_T particle in each pair. The observed ratios increase as the average pseudorapidity increases. For a given pseudorapidity, the ratios tend to remain relatively constant as a function of centrality, and typically higher than the pp reference except for the most peripheral PbPb events. These results might again reflect the influence of longitudinal hydrodynamic flow.

References

[1] R. Pasechnik and M. Sumbera, "Phenomenological review on quark-gluon plasma: Concepts vs. observations", *Universe* **3** (2017) 7, `doi:10.3390/universe3010007`, `arXiv:1611.01533`.

[2] W. Busza, K. Rajagopal, and W. van der Schee, "Heavy ion collisions: The big picture and the big questions", *Ann. Rev. of Nucl. and Par. Sci.* **68** (2018) 339, `doi:10.1146/annurev-nucl-101917-020852`, `arXiv:1802.04801`.

[3] J. Casalderrey-Solana and C. A. Salgado, "Introductory lectures on jet quenching in heavy ion collisions", *Acta Phys. Polon. B* **38** (2007) 3731, `arXiv:0712.3443`.

[4] PHENIX Collaboration, "Suppressed π^0 production at large transverse momentum in central Au+Au collisions at $\sqrt{s_{NN}} = 200\,\text{GeV}$", *Phys. Rev. Lett.* **91** (2003) 072301, `doi:10.1103/PhysRevLett.91.072301`, `arXiv:nucl-ex/0304022`.

[5] STAR Collaboration, "Direct observation of dijets in central Au+Au collisions at $\sqrt{s_{NN}} = 200\,\text{GeV}$", *Phys. Rev. Lett.* **97** (2006) 162301, `doi:10.1103/PhysRevLett.97.162301`, `arXiv:nucl-ex/0604018`.

[6] CMS Collaboration, "Overview of high-density QCD studies with the CMS experiment at the LHC", 2024. `arXiv:2405.10785`.

[7] ATLAS Collaboration, "Observation of a centrality-dependent dijet asymmetry in lead-lead collisions at $\sqrt{s_{NN}} = 2.76\,\text{TeV}$ with the ATLAS detector at the LHC", *Phys. Rev. Lett.* **105** (2010) 252303, `doi:10.1103/PhysRevLett.105.252303`, `arXiv:1011.6182`.

[8] CMS Collaboration, "Observation and studies of jet quenching in PbPb collisions at $\sqrt{s_{NN}} = 2.76\,\text{TeV}$", *Phys. Rev. C* **84** (2011) 024906, `doi:10.1103/PhysRevC.84.024906`, `arXiv:1102.1957`.

[9] ALICE Collaboration, "Measurement of jet suppression in central PbPb collisions at $\sqrt{s_{NN}} = 2.76\,\text{TeV}$", *Phys. Lett. B* **746** (2015) 1, `doi:10.1016/j.physletb.2015.04.039`, `arXiv:1502.01689`.

[10] ALICE Collaboration, "Particle-yield modification in jetlike azimuthal dihadron correlations in Pb-Pb collisions at $\sqrt{s_{NN}} = 2.76\,\text{TeV}$", *Phys. Rev. Lett* **108** (2012) 092301, `doi:10.1103/PhysRevLett.108.092301`, `arXiv:1110.0121`.

[11] CMS Collaboration, "Centrality dependence of dihadron correlations and azimuthal anisotropy harmonics in PbPb collisions at $\sqrt{s_{NN}} = 2.76$ TeV", *Eur. Phys. J. C* **72** (2012) 10052, `doi:10.1140/epjc/s10052-012-2012-3`, `arXiv:1201.3158`.

[12] CMS Collaboration, "Correlations between jets and charged particles in PbPb and pp collisions at $\sqrt{s_{NN}} = 2.76$ TeV", *JHEP* **02** (2016) 156, `doi:10.1007/JHEP02(2016)156`, `arXiv:1601.00079`.

[13] CMS Collaboration, "Pseudorapidity distributions of charged hadrons in lead-lead collisions at $\sqrt{s_{NN}} = 5.36$ TeV", 2024. `arXiv:2409.00838`.

[14] CMS Collaboration, "Description and performance of track and primary-vertex reconstruction with the CMS tracker", *JINST* **9** (2014) P10009, `doi:10.1088/1748-0221/9/10/P10009`, `arXiv:1405.6569`.

[15] CMS Collaboration, "Track impact parameter resolution for the full pseudo rapidity coverage in the 2017 dataset with the CMS phase-1 pixel detector", CMS Detector Performance Note CMS-DP-2020-049, 2020.

[16] CMS Tracker Group Collaboration, "The CMS Phase-1 pixel detector upgrade", *JINST* **16** (2021) P02027, `doi:10.1088/1748-0221/16/02/P02027`, `arXiv:2012.14304`.

[17] CMS Collaboration, "The CMS experiment at the CERN LHC", *JINST* **3** (2008) S08004, `doi:10.1088/1748-0221/3/08/S08004`.

[18] CMS Collaboration, "CMS luminosity measurement using nucleus-nucleus collisions at $\sqrt{s_{NN}} = 5.02$ TeV in 2018", CMS Physics Analysis Summary CMS-PAS-LUM-18-001, 2022.

[19] CMS Collaboration, "Precision luminosity measurement in proton-proton collisions at $\sqrt{s} = 13$ TeV in 2015 and 2016 at CMS", *Eur. Phys. J. C* **81** (2021) 800, `doi:10.1140/epjc/s10052-021-09538-2`, `arXiv:2104.01927`.

[20] CMS Collaboration, "Performance of the CMS Level-1 trigger in proton-proton collisions at $\sqrt{s} = 13$ TeV", *JINST* **15** (2020) P10017, `doi:10.1088/1748-0221/15/10/P10017`, `arXiv:2006.10165`.

[21] CMS Collaboration, "The CMS trigger system", *JINST* **12** (2017) P01020, `doi:10.1088/1748-0221/12/01/P01020`, `arXiv:1609.02366`.

[22] CMS Collaboration, "Strange hadron collectivity in pPb and PbPb collisions", *JHEP* **05** (2023) 007, `doi:10.1007/JHEP05(2023)007`, `arXiv:2205.00080`.

[23] CMS Collaboration, "Technical proposal for the Phase-II upgrade of the Compact Muon Solenoid", CMS Technical Proposal CERN-LHCC-2015-010, CMS-TDR-15-02, 2015.

[24] T. Sjöstrand et al., "An introduction to PYTHIA 8.2", *Comput. Phys. Commun.* **191** (2015) 159, `doi:10.1016/j.cpc.2015.01.024`, `arXiv:1410.3012`.

[25] CMS Collaboration, "Extraction and validation of a new set of CMS PYTHIA8 tunes from underlying-event measurements", *Eur. Phys. J. C* **80** (2020) 4, `doi:10.1140/epjc/s10052-019-7499-4`, `arXiv:1903.12179`.

[26] I. P. Lokhtin and A. M. Snigirev, "A model of jet quenching in ultrarelativistic heavy ion collisions and high-p_T hadron spectra at RHIC", *Eur. Phys. J. C* **45** (2006) 211, `doi:10.1140/epjc/s2005-02426-3`, `arXiv:hep-ph/0506189`.

[27] GEANT4 Collaboration, "GEANT4—a simulation toolkit", *Nucl. Instrum. and Meth. A* **506** (2003) 250, `doi:10.1016/S0168-9002(03)01368-8`.

[28] CMS Collaboration, "Multiplicity and transverse momentum dependence of charge balance function in pPb and PbPb collisions", *JHEP* **08** (2024) 148, `doi:10.1007/JHEP08(2024)148`, `arXiv:2307.11185`.

[29] CMS Collaboration, "Observation of long-range, near-side angular correlations in pPb collisions at the LHC", *Phys. Lett. B* **718** (2013) 795, `doi:10.1016/j.physletb.2012.11.025`, `arXiv:1210.5482`.

[30] CMS Collaboration, "Measurement of long-range near-side two-particle angular correlations in pp collisions at $\sqrt{s_{NN}} = 13$ TeV", *Phys. Rev. Lett* **116** (2016) 172302, `doi:10.1103/PhysRevLett.116.172302`, `arXiv:1510.03068`.

[31] ALICE Collaboration, "Evolution of the longitudinal and azimuthal structure of the near-side jet peak in Pb-Pb collisions at $\sqrt{s_{NN}} = 2.76$ TeV", *Phys. Rev. C* **96** (2017) 034904, `doi:10.1103/PhysRevC.96.034904`, `arXiv:1609.06667`.

[32] STAR Collaboration, "System size and energy dependence of near-side dihadron correlations", *Phys. Rev. C* **85** (2012) 014903, `doi:10.1103/PhysRevC.85.014903`, `arXiv:1110.5800`.

[33] CMS Collaboration, "Long-range two-particle correlations of strange hadrons with charged particles in pPb and PbPb collisions at lhc energies", *Phys. Lett. B* **742** (2015) 200, `doi:10.1016/j.physletb.2015.01.034`, `arXiv:1409.3392`.

[34] ALICE Collaboration, "Anomalous evolution of the near-side jet peak shape in Pb-Pb collisions at $\sqrt{s_{NN}} = 2.76$ TeV", *Phys. Rev. Lett* **119** (2017) 102301, `doi:10.1103/PhysRevLett.119.102301`, `arXiv:1609.06643`.

[35] G. Kasza and T. Csorgo, "Scaling behaviour of dn/dy in high-energy collisions", *Universe* **10(1)** (2024) 45, `doi:10.3390/universe10010045`, `arXiv:2311.18678`.

A Cross-check with ALICE published results

Figure 10: Cross-check of longitudinal width ($\sigma_{\Delta\eta}$) and transverse width ($\sigma_{\Delta\phi}$) of the near side peak with ALICE results [34].
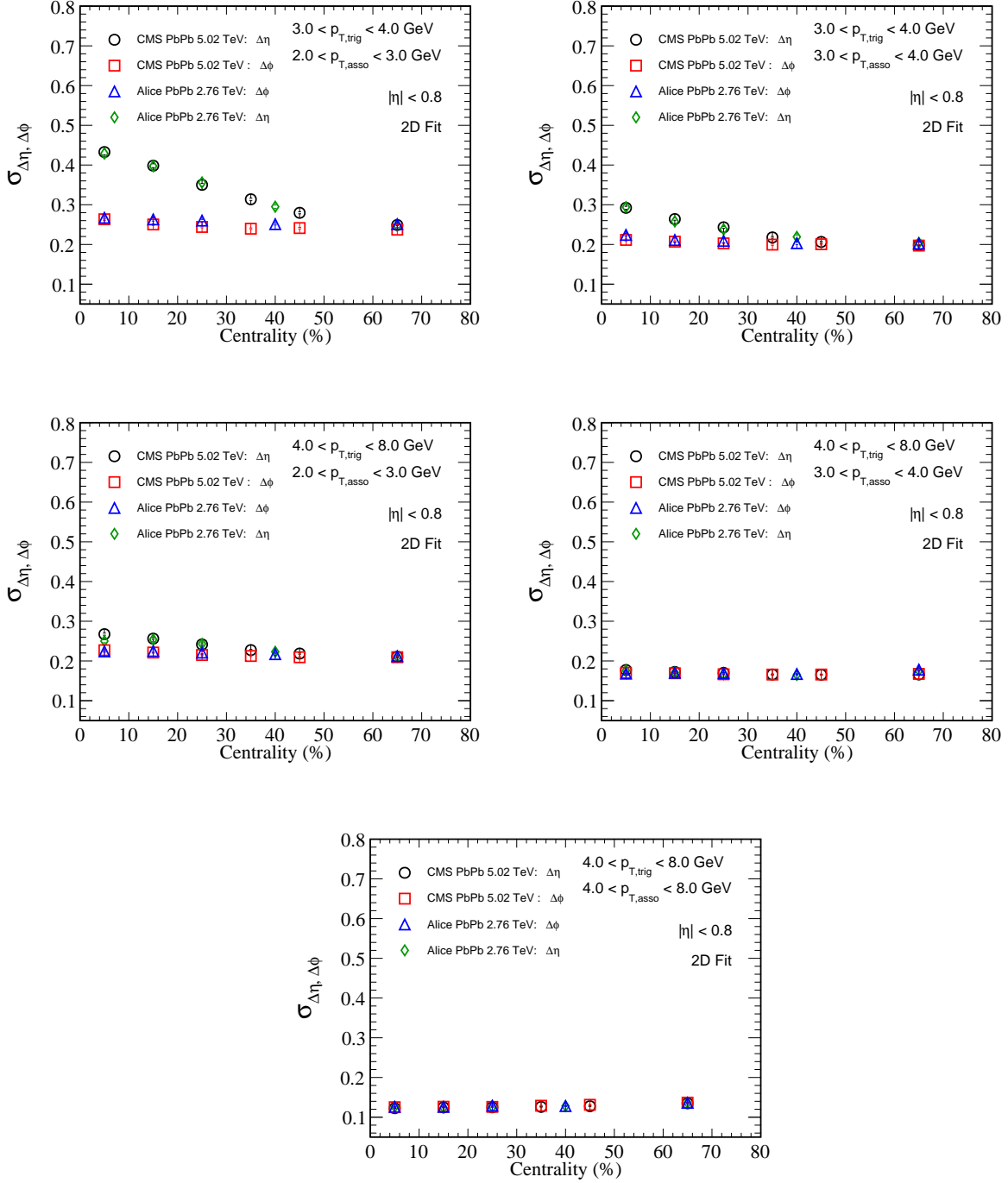
B   Comparisons between CMS $|\eta| < 0.8$ and CMS $|\eta| < 2.4$

Figure 11: Comparisons of longitudinal width ($\sigma_{\Delta\eta}$) and transverse width ($\sigma_{\Delta\phi}$) of the near side peak between CMS $\eta < 0.8$ and CMS $\eta < 2.4$ (sideband fit).